Borehole seismoelectric logging using a shear-wave source: Possible application to CO2 disposal?

Fabio Zyserman, Laurence Jouniaux, Sheldon Warden, Stéphane Garambois

Borehole seismoelectric logging using a shear-wave source: Possible application to CO_2 disposal?

This paper has been published in: International Journal of Greenhouse Gas Control, 33, 89-102, 2015

Fabio I. Zyserman[a], Laurence Jouniaux[b], Sheldon Warden[b], Stéphane Garambois[c]

[a] *CONICET, Facultad de Ciencias Astronómicas y Geofísicas, Universidad Nacional de La Plata Paseo del Bosque s/n,1900 La Plata, Argentina*

[b] *Institut de Physique du Globe de Strasbourg, UdS-CNRS UMR 7516, Université de Strasbourg, 5 rue René Descartes, 67084 Strasbourg, France*

[c] *ISTerre, Université Grenoble Alpes, CNRS UMR 5275, Grenoble, France*

Abstract

The behaviour of CO_2 deposition sites -and their surroundings- during and after carbon dioxide injection has been matter of study for several years, and several geophysical prospection techniques like surface and crosshole seismics, geoelectrics, controlled source electromagnetics among others, have been applied to characterize the behaviour of the gas in the reservoirs. Until now, Seismolectromagnetic wave conversions occuring in poroelastic media via electrokinetic coupling have not been tested for this purpose. In this work, by means of numerical experiments using Pride's equations -extended to deal with partial saturations- we show that the seismoelectric and seismomagnetic interface responses (IR) generated at boundaries of a layer containing carbon dioxide are sensitive to its CO_2 content. Further, modeling shear wave sources in surface to borehole seismoelectric layouts and employing two different models for the saturation dependence of the electrokinetic coefficient, we observe that the IR are sensitive to CO_2 saturations ranging between 10% and 90%, and that the CO_2 saturation at which the IR maxima are reached depends on the aforementioned models. Moreover, the IR are still sensitive to different CO_2 saturations for a sealed CO_2 reservoir covered by a clay layer. These results, which should be complemented by the analysis of the IR absolute amplitude, could lead, once confirmed on the field, to a new monitoring tool complementing existing ones.

Keywords: Permeability and porosity, Numerical approximations and analysis, Wave propagation, Acoustic

properties, Electrical properties, Electrokinetic, Seismoelectric, Seismomagnetic

1. Introduction

Injection of large amounts of man-produced CO_2 in depleted oil wells below the sea floor and in other apropriate geological formations has been used, for several years, as a means of reducing the carbon dioxide emissisons into the atmosphere. For example, CO_2 is being injected in the Sleipner field in the North Sea since 1996 at a rate of 0.85 Mt per year (Ellis, 2010), and also beneath the Sahara desert, at In Salah in Algeria (Ringrose et al., 2009). The former has been a subject of extensive theoretical and experimental studies, including laboratory rock sample analysis, seismic monitoring, etc. We mention, from the large literature concerning this deposition site, the studies of Chadwick et al. (2009, 2010) where time-lapse seismic is employed to characterize CO_2 plume development, and the studies of Gomez and Ravazzoli (2011), where CO_2 content related to seismic attributes were investigated. Moreover, a test site in Ketzin, Germany, is being run and extensively studied in order to monitor the CO_2 behaviour during injection and afterwards, see Martens et al. (2012, 2013) and references therein. Scientists from different areas have been studying this topic, and a still open problem is to predict the behaviour of the gas once set into the reservoir. Will it remain stable? Will it migrate, and make its way back to the surface? How the stored CO_2 can be efficiently monitored in order to avoid pollution of overlying aquifers by leaked gas, among other issues (Thibeau and Mucha, 2011) is still a topic of intense research.

Among other works implemented at Ketzin, Wiese et al. (2010) studied the hydraulic properties of the storage reservoir, Kazemeini et al. (2010) carried out some rock physics and seismic modeling studies of surface seismic CO_2 monitoring, and cross-well seismic tomography has been also performed (Zhang et al., 2012); more recently Fischer et al. (2013) made laboratory studies of geochemichal changes induced in Ketzin rock matrix samples by the presence of the stored carbon dioxide, and Wiese et al. (2013) studied -at the same site- not only the geochemical but also the hydraulic changes induced in the overburden by deposited CO_2. We can also mention that both seismic and electric methods are potentially appropriate to study the CO_2 reservoir

(Fabriol et al., 2011; Girard et al., 2011; Carcione et al., 2012). Martens et al. (2012) describe not only the results of different campaigns including seismic, surface and borehole monitoring, but also some seismic simulation runs in order to check previous models; on the other hand synthetic and field geoelectrical methods were applied to study possible gas migration (Kiessling et al., 2010). Moreover Ishido et al. (2013) have numerically investigated the application of self potential methods to monitor the migration of CO_2 sequestrated into saline aquifers, concluding that the used methods are effective for sensing the approach of CO_2 to the well casings deep within the subsurface. We finally point out that in recent studies it was shown that seismics was useful to detect CO_2 saturation below 15% and that electrical resistivity was useful to detect CO_2 saturation above 15% (Kim et al., 2013).

Seismoelectric signals are electrokinetically generated by the propagation of seismic waves within a porous material. They can be recorded using a seismic source and electric receivers. The seismoelectric strategy aims to combine the resolution of the seismics to the sensitivity of the electric methods to fluid content. A specific seismoelectric signal, denoted the interfacial response, is expected to be induced at contrasts between rock properties (Garambois and Dietrich, 2002), including different fluids and different fluid-contents. This signal is usually weak compared to the so-called coseismic signal, which is the seismo-electric signal travelling within the seismic wave directly induced by the source. Several authors have investigated the benefits of surface-to-borehole seismoelectric layouts to accomplish efficient measurements of the interfacial response, as opposed to layouts for which both the seismic source and the receiving electrodes are laid at the surface.

The aim of this work is to provide numerical evidence that borehole seismoelectrics can discern carbon dioxide concentrations in a broader range than seismics allow, detecting at the same time salinity contrasts, task up to now fulfilled by geolectrics. The pure SH seismic source considered in the present study could achieve a better resolution than the one obtained through the usual P-driven experiments because of shorter wavelengths. We start our work by reviewing the most important theoretical concepts of seismoelectrics, and by proposing a possible appropriate field experimental setup. We follow by analyzing shear-wave driven interface responses generated between to two consecutive units saturated with water, using a one dimensional finite element method to approximate the solution to Pride's equations. We study the sensitivity of these responses to contrasts in

relevant parameters, such as porosity, salinity and viscosity; and continue by investigating the coseismic waves and interface response amplitudes of tabular media when one layer is partially saturated with carbon dioxide, employing in this analysis different models to take into account this situation in the electrokinetic coupling. Finally, we consider a layered model including a seal layer, in order to simulate a realistic CO_2 deposition site.

2. Theoretical background

The seismoelectric method relies on electrokinetically induced seismic-to-electric energy conversions occurring in fluid-containing porous media. The reader can find a tutorial on electrokinetics in Jouniaux and Ishido (2012).

2.1. Theoretical aspects

When a compressional wave travels through a porous medium, it creates a fluid-pressure gradient and an acceleration of the solid matrix, inducing a relative motion between the immobile ions adsorbed at the grain surface and the counter-ions in the diffuse layer. This charge separation at the scale of the seismic wavelet creates an electrical potential difference known as the streaming potential. The electric field arising from this potential is known as the coseismic wave, as it travels within the passing compressional seismic waves. Therefore coseismic electric fields do not extend outside the seismic waves creating them, and may only help characterize the medium near the receivers. For borehole seismoelectric measurements they give information about the medium in the vicinity of the well (Mikhailov et al., 2000).

Another type of seismoelectric conversions arises when a seismic wave crosses a contrast between mechanical or electrical properties (Haartsen and Pride, 1997; Chen and Mu, 2005; Block and Harris, 2006). In this situation a transient localized charge separation across the interface is created, which acts as a secondary source that can be approximated as an electrical dipole oscillating at the center of the first Fresnel zone (Thompson and Gist, 1993; Garambois and Dietrich, 2002). The resulting electromagnetic (EM) wave is known as the interface response (IR), and diffuses independently from the seismic wavefield: the velocity at which it travels is several orders of magnitude greater than seismic velocities. This IR may provide information about the contrasts in the medium's properties at depth.

The equations governing the coupled seismic and electromagnetic wave propagation in fluid-filled porous media were derived by Pride (1994) by combining Maxwell's equations with Biot's equations for poroelasticity (Biot, 1956a,b). Two coupled transport equations were derived (Eq.251 and 252 in Pride (1994)):

$$\mathbf{J} = \sigma(\omega)\mathbf{E} + L(\omega)\left(-\nabla p + \omega^2 \rho_w \mathbf{u_s}\right) \tag{1}$$

$$-i\omega\mathbf{u_f} = L(\omega)\mathbf{E} + \frac{k(\omega)}{\eta_w}\left(-\nabla p + \omega^2 \rho_w \mathbf{u_s}\right) \tag{2}$$

The macroscopic electrical current density $\mathbf{J}$ [A/m^2] is given in Eq.1 as the sum of the average conduction and streaming current densities, respectively the first and second term of its right-hand side. Both the above equations assume a $e^{-i\omega t}$ time dependence of the propagating wave, where ω [rad/s] denotes the angular frequency. The parameter $\mathbf{E}$ [V/m] denotes the electric field and $\sigma(\omega)$ [S/m] is the frequency-dependent conductivity of the material. Streaming currents may be induced by both the pressure gradient $-\nabla p$, where p [Pa] is the pore-fluid pressure, and the acceleration of the solid frame $\omega^2 \rho_w \mathbf{u_s}$, where ρ_w [kg/m^3] is the density of the fluid (water) and $\mathbf{u_s}$ [m] denotes the solid displacement. The fluid velocity $-i\omega\mathbf{u_f}$ [m/s] is written in Eq.2 as the sum of electrically and mechanically induced contributions. The frequency-dependent permeability is written as $k(\omega)$ [m^2] and the dynamic viscosity of the fluid is expressed as η_w [Pa.s]. The complex and frequency-dependent coupling $L(\omega)$ links Eq.1 and Eq.2:

$$L(\omega) = L_0 \left[1 - i\frac{\omega}{\omega_t}\frac{b}{4}\left(1 - 2\frac{d}{\Lambda}\right)^2 \left(1 - i^{3/2} d \sqrt{\frac{\omega\rho_w}{\eta_w}}\right)^2\right]^{-\frac{1}{2}} \tag{3}$$

In Eq.3, Λ [m] is a pore geometrical parameter, defined in Johnson et al. (1987), whereas b is a dimensionless parameter defined in terms of the latter, the porosity ϕ, the absolute permeability k_0 and the tortuosity α_∞ as b=$\frac{\phi}{\alpha_\infty k_0}\Lambda^2$ and consisting only of the pore-space geometry terms. This parameter b was originally denoted m in Pride (1994). When k_0, ϕ, α_∞ and Λ are independently measured, b is comprised between 4 and 8 for a variety of porous media ranging from grain packing to capillary networks consisting of tubes of variable radii (Johnson et al., 1987). The parameter d [m] denotes the Debye length, while ω_t [rad/s] is the permeability-dependent transition angular frequency between the low-frequency viscous flow and high-frequency inertial flow. Finally, L_0 denotes the electrokinetic coupling which expression we give below. The coupling $L(\omega)$ was studied by

Reppert et al. (2001), Schoemaker et al. (2007), Jouniaux and Bordes (2012) and Glover et al. (2012). When this coefficient is set to zero, the two subsets of equations describing the behavior of EM and seismic waves are decoupled. Different modellings have been developed to resolve the seismoelectric conversions, see for example (Guan et al., 2013; Schakel et al., 2012, 2011; Gao and Hu, 2010; Guan and Hu, 2008).

2.2. Transfer functions

The displacement and EM fields in an isotropic and homogeneous wholespace were derived by Pride and Haartsen (1996) using a plane-wave solution of the governing equations. Later, Garambois and Dietrich (2001) making use of these results, derived the electric and magnetic fields $\mathbf{E}$ and $\mathbf{H}$ as a function of the seismic displacement $\mathbf{u}$. They demonstrated that low-frequency approximations of these relationships lead to a seismoelectric field $\mathbf{E}$ proportional to the grain acceleration $\ddot{\mathbf{u}}$ associated to longitudinal fast $P-$waves as:

$$\mathbf{E} \simeq \frac{\epsilon_0 \kappa_w \zeta}{\eta_w \sigma_w} \, \rho_w \left(1 - \frac{\rho}{\rho_w}\frac{C}{H}\right) \ddot{\mathbf{u}} = C_K \, \rho_w \left(1 - \frac{\rho}{\rho_w}\frac{C}{H}\right) \ddot{\mathbf{u}}; \tag{4}$$

moreover, Garambois and Dietrich (2001) verified the consistency of this relation on real field P-wave volume waves. The definitions of the C and H moduli are those of Biot (1962); ϵ_0 is the vacuum permittivity, κ_w and σ_w are the dimensionless dielectric constant and the electrical conductivity of the saturating fluid respectively. The zeta potential ζ [V] is the electric potential on the sliping plane within the electric double layer.

Therefore the coseismic electric field is also proportional to the electrokinetic coefficient C_K largely studied in laboratory and modeled (Vinogradov and Jackson, 2011; Vinogradov et al., 2010; Aizawa et al., 2008; Guichet et al., 2006; Maineult et al., 2006; Jouniaux et al., 1999; Pozzi and Jouniaux, 1994; Jouniaux et al., 1994; Ishido and Mizutani, 1981).

The magnetic field $\mathbf{H}$ has been shown to be proportional to the velocity $\dot{\mathbf{u}}$ associated to transverse SH- and SV -waves as:

$$\mid \mathbf{H} \mid \simeq \frac{\phi}{\alpha_\infty} \, \frac{\varepsilon_0 \, \kappa_w \, |\zeta|}{\eta_w} \, \rho_w \sqrt{\frac{G}{\rho}} \, |\dot{\mathbf{u}}| \tag{5}$$

where G is the shear modulus of the framework. The tortuosity α_∞ is usually taken equal to the product of the porosity by the formation factor F. The magnetic field can also be expressed as a function of the electrokinetic

coefficient C_K as:

$$| \mathbf{H} | \simeq \frac{\varepsilon_0 \kappa_w |\zeta|}{\eta_w \sigma_w} \frac{\sigma_w}{F} \rho_w \sqrt{\frac{G}{\rho}} |\dot{\mathbf{u}}| = C_K \frac{\sigma_w}{F} \rho_w \sqrt{\frac{G}{\rho}} |\dot{\mathbf{u}}| \quad (6)$$

Therefore the coseismic magnetic field is also proportional to the electrokinetic coefficient, considering that the water density and conductivity are constant, as are the formation factor and the G, C, H moduli.

3. Appropriate field experimental setup

Although performing a field experiment is beyond the scope of this paper, we would like to emphasize what would be the most appropriate geometry to be developed to detect seismo-electromagnetic conversions for CO_2 disposal monitoring. The interfacial response can provide information about the formations at depth while the co-seismic signal provides only information of the soil in the vicinity of the electrodes. The challenge is therefore to isolate the interfacial response, which is often of the order of 1-100 μV/m (Mikhailov et al., 2000; Chen and Mu, 2005; **?**).

3.1. Signal processing

The first step in processing the seismoelectric data is to remove the noise from power lines, which can be of the order of 1 mV/m. The estimate of the harmonic noise can be performed on the data recorded just before the shot, using a pre-trigger recording. The filtering of this noise can be performed by applying a single frequency adaptative noise cancellation filter. Butler et al. (1996) proposed to apply the techniques of block and sinusoidal substraction. Presently the most efficient method which is used for most of the observations is to routinely reduce the harmonic noise using the algorithm of Butler et al. (1996); Butler and Russell (2003); Butler et al. (2007) applied to individual shots before the stacking. Wiener and bandpass filters can be used to reduce high-frequency noise. Supplementary techniques as delay-line filtering in case of severe noise, and low-pass filtering in case of strong high-frequency noise contamination can be used.

3.2. Benefit of surface-to-borehole measurements

The main issue for detecting the weak IR signal is often the high amplitude of the co-seismic signal. We propose to perform the electromagnetic measurements in borehole so that this IR signal can be recorded before

the arriving of the co-seismic signal. Indeed the interfacial response can be observed free from the coseismic signal when the electrodes are located below the interface of interest (Dupuis et al., 2007), by measuring the electric field within a borehole. In (Haines, 2004; Haines et al., 2007) field experiments were conducted in which the source and the receivers were laid on opposite sides of one or two man-made sand-filled trenches dug in a clayey background. This fan-shape layout enabled the measurement of the Interface Response as it reached the electric receivers before the typically stronger Coseismic wavefield. Therefore, the authors suggested that by setting the source at the surface and the electrodes in a borehole *below* the interfaces of interest, one may separate the different types of seismoelectric waves without resorting to numerical wave separation techniques. This layout-related separation may better preserve the amplitudes and waveforms of seismoelectric signals than numerical data processing such as f-k or $\tau - p$ filtering, often distorting seismoelectric signals (Warden et al., 2012). Moreover, with this layout the influence of surface waves is strongly decreased; however Stoneley waves may appear; which should be dealt with.

Another benefit of surface-to-borehole geometries is related to the amplitudes of the Interface Response. When working with surface geometries, deep interfaces become rather harder to track as the amplitudes of the associated interfacial signals may have decayed below the noise level by the time they reach the surface. Setting the receivers close to the target interfaces therefore allows to pick up stronger signals (Haines and Pride, 2006). Furthermore, when working with uncased wells (Zhu et al., 1999), deploying the receivers at depth also allows to take advantage of the Coseismic signal, which provides information about the subsurface in the vicinity of the receivers (Garambois and Dietrich, 2001; Haines et al., 2007; Bordes et al., 2008). For instance, by hitting the upper casing of a borehole with a sledgehammer, Mikhailov et al. (2000) triggered Stoneley waves, which in turn induced a pore fluid flow in the permeables zones intersecting the borehole. The authors were able to measure the small (tens of microvolts) electrical signals associated with this flow.

3.3. Seismic source

We propose to use a pure SH seismic source that could achieve a better resolution than the one obtained through the usual P-driven experiments because of shorter wavelengths. As stated in Haines and Pride (2006), there is no coseismic electric field for S-waves, but the coseismic magnetic field is present; therefore the electric

IR may be easier to be detected than the magnetic IR.

In the next sections, we use a 120 Hz peak frequency for the source to keep the response in time fairly sharp, so that the different events could be easily resolved. But, as for the whole range of seismic frequencies both the dynamic permeability and the electrokinetic coupling coefficient are fairly independent of the frequency, qualitatively the same responses would be obtained for a source with peak frequency of 40 Hz or 60 Hz. A pure shear wave source is difficult to achieve; however surface vibrators for SH-source do exist, which can emit SH-waves as well as SV-waves, being designed for a peak force of approximately 30 kN (equivalent to the free fall of a 3 t mass from a height of 1 m) and a frequency range of 16 Hz to 300 Hz.

Furthermore, there is presently interest in the seismics community in S-wave exploration because of its application in unconventional reservoirs; an application in heavy oil production management through S-wave data monitoring of stress effects in the reservoir has been reported (Bale et al., 2013), as well as monitoring of the seal of a CO_2 deposition site (Davis et al., 2013). This situation could contribute to facilitate further progress in field measurements in seismoelectrics using shear wave sources.

4. Modeling seismoelectric and seismomagnetic signals measured at depth using a shear-wave source

In this section we use a numerical simulator, which features infinite shear sources generating 1D wave fields in likewise layered media for the modeling of the seismoelectric conversions; see the appendix for details in the 1D SHTE formulation. We model the seismoelectric and seismomagnetic conversions induced by a shear-wave source within a tabular model consisting of a sand layer over a sandstone layer. We then describe the results of the horizontal displacement, the horizontal electric field, and the horizontal magnetic field as a function of depth for full water saturation conditions.

4.1. Model description

We consider a simple tabular model consisting of a sand layer, 30.5 m thick, set on top of a sandstone half-space (Fig. 1).

We model a seismic transverse source of peak frequency f_{peak}=120 Hz at a depth of z_s=1 m, the source wavelet being a Ricker wavelet, or "Mexican hat" wavelet, which generates seismoelectric signals recorded by a vertical

array located right under the source; this array consists of 51 seismic and electromagnetic transverse receivers, evenly spaced between a depth of 1 and 51 m so that there are receivers on either side of the interface.

The considered source is just a shearing force per unit volume applied along y on a whole horizontal plane located at the source depth with the already described signature, its implementation can be seen in the appendix.

Both sand layer and sandstone layer -called Sand and Sandstone I in Table 1, where their properties are detailed- are fully saturated with a moderately briny water (C_0=10^{-3} mol/L). As there is no salinity contrast between the two layers and since we compute the ζ potential as $\zeta = 0.008 + 0.026 \log_{10}(C_0)$ (Pride and Morgan, 1991), ζ=-70 mV throughout the entire model. The frame bulk modulus K_{fr} [Pa] is deduced from the solid bulk modulus K_s [Pa], following Pride (2005) and assuming a consolidation parameter of 20 for sand and 5 for sandstone as

$$K_{fr} = K_s \frac{1-\phi}{1+c_s\phi}. \tag{7}$$

The frame shear modulus G_{fr} [Pa] is linked to the solid shear modulus modulus G_s in a similar fashion:

$$G_{fr} = G_s \frac{1-\phi}{1+1.5c_s\phi}. \tag{8}$$

As we deal in next sections with porous media saturated with mixtures of water and CO_2, it is necessary to introduce appropriate effective properties in order to use them within Pride's formulation for electroseismics. Therefore, for the effective fluid mass density we use

$$\rho_f = \rho_w S_w + \rho_{CO_2}(1 - S_w), \tag{9}$$

where $S_w + S_{CO_2} = 1$ is assumed and subscripts CO_2 and w refer to carbon dioxide and water respectively, S_w denotes water saturation. For the effective bulk modulus of such fluid mixture we use Brie et al. (1995) approach

$$K_f = (K_w - K_{CO_2})S_w^5 + K_{CO_2}; \tag{10}$$

the power five in this expression is chosen following Carcione et al. (2006). Here the CO_2 is supercritical as explained in the section 6 and there is no gaseous phase in our model. The effective viscosity is computed in terms of the mixture components viscosities $\eta_l,\ l = w, CO_2$ and water saturation S_w using Teja and Rice

(1981)

$$\eta_f = \eta_{CO_2} \left(\frac{\eta_w}{\eta_{CO_2}} \right)^{S_w}. \tag{11}$$

In order to characterize the electric conductivity of the effective fluid saturated solid matrix we use the expression recently proposed by Warden et al. (2013), extending Pride's original formula (Pride, 1994, Eq.(242)) to the realm of partially saturated media:

$$\sigma(S_w, \omega) = \frac{S_w^n}{F}\sigma_w + \frac{2}{F}\frac{C_{em} + C_{os}(\omega)}{\Lambda} \tag{12}$$

The first term in this equation -where $F = \phi^{-m}$ stands for the formation factor, m being the cementation coefficient- is Archie's law for a partially saturated medium, while the second term accounts for the surface conductivity. In the latter, -as Pride stated in his liminar work- the factor C_{em} [S] is the excess conductance associated with the electromigration of double layer ions; $C_{os}(\omega)$ [S] is the frequency-dependent electro-osmotic conductance due to electrically induced streaming of the excess double-layer ions and Λ [m] is the above presented pore-geometry dependent factor. We remark here that, as in Brovelli et al. (2005)and Warden et al. (2013), the surface conductivity is assumed to be independent of water saturation S_w, because under realistic saturation ranges (residual water saturation $S_{wr} \geq 10\%$) the thickness of the wetting phase layer on the pore surface is always larger than the Debye length d. This also means that all fluid related properties involved in the calculation of the surface conductivity and of the electrokinetic coupling -see below- are just those of water. Again, following Warden et al. (2013), we propose for the effective fluid saturated media the following electrokinetic coupling:

$$L_0(S_w) = -\frac{\phi}{\alpha_\infty}\frac{\epsilon_0 \kappa_w \zeta}{\eta_w}(1 - 2\frac{d}{\Lambda})S_w^n S(S_w), \tag{13}$$

In this equation n is Archie's saturation exponent (taken to be equal to the cementation exponent) and $S(S_w)$ is a function relating the streaming potential coefficient obtained under partial saturation conditions to the one corresponding to full saturation conditions. Several authors investigated this relation from both theoretical and experimental viewpoints; Perrier and Morat (2000), Guichet et al. (2003), Revil et al. (2007), and Strahser et al. (2011) predict a monotonic behaviour with saturation, Jackson (2010) suggested that the coupling coefficient could be either monotonic or non-monotonic depending on the properties of the saturating phases, while

Allègre et al. (2010) and Allègre et al. (2012) observed and modeled a non-monotonic behaviour while studying laboratory drainage experiments; we select for the present work two expressions for $S(S_w)$ displaying a qualitatively distinct behaviour, meaning monotonic and non-monotonic:

$$S(S_w) = \begin{cases} \frac{1}{S_w^n}\left(\frac{S_w - S_{wr}}{1 - S_{wr}}\right)^2 & S_{wr} = 0.10 \quad \text{(Perrier and Morat, 2000)} \\ \left(\frac{S_w - S_{wr}}{1 - S_{wr}}\right)\left(1 + 32\left(1 - \left(\frac{S_w - S_{wr}}{1 - S_{wr}}\right)\right)^{0.4}\right) & S_{wr} = 0.305 \quad \text{(Allègre et al., 2010).} \end{cases} \tag{14}$$

4.2. Seismic and seismo-electromagnetic results

In this section we present our first results; here it should be noticed that they correspond to media saturated with water, i.e. $S_{CO_2} = 0$, and that free surface reflections are neglected.

On the synthetic recording displaying the horizontal solid displacement (Figure 2 (a)), one can notice the downgoing direct S-wave $u_{y,i}$, traveling at v_S = 1104 m/s. When this direct wave hits the interface located at 30.5 m depth at about 0.027 s, part of the total incident energy reflects back to the surface as an upgoing S wave $u_{y,r}$ with the same velocity as the incident wave. The transmitted downgoing S wave $u_{y,t}$ travels at a higher velocity of v_S = 2485 m/s.

On the synthetic recording displaying the horizontal electric field (Figure 2 (b)), one can distinguish three events. An event with zero moveout -labeled as E_D in this figure- appears at the time at which the source is triggered (0.01 s). This flat arrival may be related to the *direct field* predicted by Pride and Haartsen (1996) and measured by Haines (2004).

An event we associate with a first Interface Response -E_{IR} in the figure- arises at about 0.027 s, that is, at about the time needed for the S-wave to reach the interface. A second Interface Response E_{IR2} occurring at the surface when the S-wave reflected at the 30.5 m deep interface $u_{y,r}$ reaches the surface, is seen at two-way traveltime. Its origin could be partially due to an numerical artifact caused by the boundary conditions for Biot equations at the Earth surface; further modelling with independent codes and field experiments will help to clarify this question.

It is also interesting to notice that, as stated in Haines and Pride (2006), there is no coseismic electric field for S-waves, but the coseismic magnetic field is present, as can be seen in Figure 2 (c). The magnetic field existing within the seismic shear wave displays the same behaviour as the latter: the incident coseismic magnetic field

$H_{C,i}$ arrives at the 30.5 m depth interface at about 0.027 s, and is partially transmitted -see $H_{C,t}$ in the figure-, and partially reflected towards the surface as $H_{C,r}$. It is also possible to see the flat event associated to the direct field H_D, at about 0.01 s, and a first Interface Response H_{IR} generated simultaneously with the arrival of the seismic wave to the interface. The amplitude of the Interface Response is negligible in the upper layer. Finally, the second Interface Response occurring at the Earth surface, labeled H_{IR2} in the figure, is also present for the magnetic field.

5. Sensitivity of the Interface Response to contrasts in fluid and rock properties

In this section we describe the amplitude of the interfacial reponse induced by a S-wave source when some physical properties of the sandstone half-space are changed whereas an upper sandstone layer is kept with constant parameters.The properties of the upper sandstone layer (Sandstone II) are given in the third column of Table 1.

5.1. Porosity contrast

In this paragraph we study the influence of a porosity contrast on the amplitude of the interfacial response. The porosity in the lower half-space is allowed to change between 2 and 24%. The empirical relation of Bourbié et al. (1987) linking porosity and permeability in Fontainebleau sandstones is used to account for the influence of porosity changes on permeability,

$$k_0 = 1.66 \times 10^{-4}\phi^8 \text{ for } \phi < 6\% \tag{15}$$

$$k_0 = 2.5 \times 10^{-10}\phi^3 \text{ for } \phi > 6\% \tag{16}$$

The permeability values associated with the porosity values of the sandstone half-space are given in Table 2. For each set porosity and permeability values, we modeled the electric field along y, and measured the maximum S-EM IR value on the synthetic electrograms. Apart from porosity and permeability varying in the lower half-space, all other parameters are fixed.

In order to eliminate the influence of the source amplitude, the results obtained were normalized as follows: for

each fixed parameter (here porosity) value, the portion of the signal corresponding to the interfacial response is isolated, and the maximum value of the maximum amplitude of all recorded IR's is selected. By varying the analysed parameter a set of these maxima is obtained. Finally, this set is normalised by dividing all values by the maximum value in it. The obtained results are displayed in Figure 3. When the porosity value of the sandstone layer is 12%, meaning the same value as the upper sand layer, the interfacial response is zero because there is no contrast of any physical properties between the layers. When the porosity of the sand layer is either decreasing down to 2% or increasing up to 24% the maximum amplitude is increasing, because the contrast in porosity between the two layers is increasing.

5.2. ζ potential contrast

Following the same procedure as in the previous paragraph, we investigate the behaviour of the S-EM IR response when the ζ potential in the top layer remains fixed at -0.035V, whilst its values are allowed to vary from -0.05V to -0.07V in the half-space.

Results are shown in Figure 4: when both layers have the same zeta potential, there is no contrast in physical properties to induce an interfacial response. When the contrast in the zeta potential is increased, either by decreasing or increasing the zeta potential of the lower layer, then the interfacial response is increased.

5.3. Viscosity contrast

We finish this section by studying the dependence fo the S-EM IR response when the viscosity $\eta = 10^{-3}$ Pa.s in the upper-layer, whilst its values are allowed to vary from to 10^{-4} Pa.s to 10^{-1} Pa.s in the half-space. Results are displayed in Figure 5. As for the study of the other properties, when there is no contrast in physical properties there is no interfacial response. When the constrast in viscosity is increasing between the layers, the amplitude of the interface response increases. However, when the viscosity of the half space is larger than that of the upper layer, the amplitude of the response grows slowly, contrary to what happens when the viscosity of the half space is smaller than that of the top layer.

This sensitivity study shows that the amplitude of the interfacial response increases with an increasing contrast in porosity and zeta potential. This amplitude is also increased by an increasing contrast in viscosity when viscosity is decreased, which is the case when dealing with CO_2 at supercritical conditions.

6. Effect of a contrast between water-saturated sand and sandstone with various CO_2 saturations

In this section we model a contrast between an upper water-saturated layer and a lower semispace with various concentrations of CO_2 at supercritical conditions. We describe the results of the modelling coseismic magnetic field and the electric and magnetic interfacial responses induced by a shear-wave source.

6.1. Model including a layer with various CO_2 concentrations

In this section we consider a simple model which consists of a 100 m thick layer on top of a half-space. Whilst the top layer remains fully saturated with water with a salinity coefficient $C_0 = 10^{-3}$ mol/l, the CO_2 saturation is allowed to vary in the half-space; the salinity is the same in both layers. The effective properties necessary for Pride's equations to remain valid when dealing with more than a single fluid phase are calculated following the formulae described in Section 4.1. As it is known from the CO_2-sequestration literature, see - among others- (Kiessling et al., 2010; Cairns et al., 2012), this gas is usually pumped in a supercritical state into the subsurface. Therefore, we assume here that CO_2 is in the mentioned supercritical state and throughout the next sections we consider the following physical properties values for the carbon dioxide $\rho_{CO_2} = 505$ kg/m^3, $\eta_{CO_2} = 1.5 \times 10^{-4}$ Pa.s, $K_{CO_2} = 25$ MPa, (Carcione et al., 2006) which as just mentioned correspond to it being in supercritical state meaning at pressure 10 MPa and temperature 37 ^{o}C.

Although a hundred meters depth are not enough for this assumption to be valid (Kazemeini et al., 2010), we retain the mentioned depth value to keep a reasonable computational cost, because of the size of the model. Note that the following analysis would remain exactly the same if we increased the depth of the bottom of the top layer as much as necessary to reach the pressure and temperature conditions for the CO_2 to be in supercritical state.

It is known that when pumped into a reservoir a small portion of carbon dioxide dissolves in water (Carcione et al., 2006; Wang et al., 2013), forming weak carbonic acid which reacts with the present dissolved salt ions (Darwish and Hilal, 2010). This process alters the ζ potential (Moore et al., 2004), which in turn changes the electrokinetic coupling L_0; in the present work the zeta potential itself is not varying, but the effect of water-saturation is taken into account, as described above, by making L_0 saturation dependent. We assumed that the electrokinetic coupling is changed when the amount of CO_2 is increased and water expelled, as it changes when

water-saturation is decreased, replaced by air (Eq.13).

We remark here that, as it can be inferred from Equation (12), we consider the electrical conductivity of carbon dioxide σ_{CO_2} negligible compared to that of salty water. Although the CO_2 is not gaseous in our model, the supercritical CO_2 will increase the electrical resistivity of the layer, compared to water, as will do the air, with a lower increase induced by supercritical CO_2 than by gaseous CO_2 (Borner et al., 2013). Further studies should investigate, if possible, the electrokinetic coefficient in presence of supercritical CO_2.

6.2. Results of the modelling: coseismic magnetic field

We first model the coseismic signal linked to the seismic propagation induced by the S-wave source (Fig.6a). The maximum of each trace, as a function of depth, is pointed, and the maximum of these maxima is deduced, for each CO_2 saturation. Then this maximum is normalized by the value of the magnetic field for water-saturated conditions, each curve being normalized by its own maximum value. When no CO_2-dependence on L_0 is assumed, meaning $S_w^n S(S_w) = 1$ in Eq.13, the coseismic magnetic field linearly decreases with increasing CO_2 content. Even when L_0 remains constant, as the effective fluid density and conductivity diminish with increasing CO_2 saturation, so does the coseismic magnetic response, as can be seen from Fig.6a, reflecting the behaviour predicted in Eq. 6.

When assuming a monotonous decrease of the electrokinetic coefficient with decreasing water-saturation as proposed by Perrier and Morat (2000), it is expected to observe a monotonous decrease of the coseismic magnetic field $\mathbf{H}$ as foreseen in Eq.6 and shown in fig.6a. Then, when another behaviour of the electrokinetic coefficient as a function of the water-saturation is assumed, as the one proposed by Allègre et al. (2010), we can observe first an increase in the coseismic magnetic field when the CO_2 saturation is increased and then a decrease with further increasing CO_2 saturation, as expected through the Eq.6 where the magnetic field is proportional to the electrokinetic coefficient.

6.3. Results of the modelling: electric and magnetic interfacial responses

The interfacial response of the electric field and the magnetic field are shown in figures 6b and 6c. The electric interfacial response is increasing with increasing CO_2 saturation, for both cases of $S_w^n S(S_w) = 1$ and

for the model from Perrier and Morat (2000). Using the model of Allègre et al. (2010) the electric interfacial response first increases to reach a maximum for a CO_2 saturation of about 12% and then decreases for a CO_2 saturation in the range 12-55% before increasing for a CO2 saturation in the range 55-70%. The magnetic interfacial response increases when the CO_2 saturation increases up to about 70% for both cases of $S_w^n S(S_w) = 1$ and for the model from Perrier and Morat (2000), before decreasing with further increase of CO_2 saturation. Using the model of Allègre et al. (2010) the magnetic interfacial response first increases to reach a maximum for a CO_2 saturation of about 10% and then decreases for a CO_2 saturation in the range 10-55% before increasing for a CO2 saturation in the range 55-70%. Therefore the relative maximum interfacial response, for both the electric field and the magnetic field, is different according to the different models of the CO_2-dependence of the electrokinetic coupling, and occurs either around 10% or 70-90% of CO_2 saturation.

We can compare the behaviour of the interfacial response of the electrical field observed here with the one observed for the study of a contrast in water-saturation using a P-wave source rather than a S-wave source (Warden et al., 2013). The electric interfacial response showed also an increase and then a decrease with increasing air-content using the model of Allègre et al. (2010), but showed a maximum at about 30% (Fig.9a in Warden et al. (2013)) rather than 12% (see Fig6b). The electrical interfacial response using the model of Perrier and Morat (2000) also showed a continuous increase with increasing air-content, although the curvatures are different.

These results do not show the relative amplitudes according to the different models. Consequently we normalized the magnetic coseismic field, the electric interfacial response and the magnetic interfacial response obtained for both models by the field values obtained using the electrokinetic coupling L_0 assuming $S_w^n S(S_w) = 1$ in Eq.13. These results show that the amplitude of the coseismic magnetic field using the model from Allègre et al. (2010) can be a factor 10 larger than the results using the model from Perrier and Morat (2000) for CO_2 saturation around 10% (fig.7). The electric interfacial response using the model from Allègre et al. (2010) can be about 50 times larger than the results using the model from Perrier and Morat (2000) for CO_2 saturation around 5% (fig.8). The magnetic interfacial response using the model from Allègre et al. (2010) can be also about 50 times larger than the results using the model from Perrier and Morat (2000) for CO_2 saturation around 5% (Fig.9). Comparing figures 7 and 9 we can deduce that the ratio between the IR amplitude and coseismic

amplitude of the magnetic field is about 45 and 6 using the model from Allègre et al. (2010) and Perrier and Morat (2000) respectively.

We can notice that in both considered cases for the CO_2-dependence of the electrokinetic coupling model, the magnetic IR is larger than the coseismic magnetic field, which is not usually the case for the electric field using a P-wave source. Therefore measuring the magnetic interfacial response induced by a S-wave source, could be an efficient method to detect the interface between a water-saturated layer and a partially CO_2 saturated layer. Moreover, as the electric coseismic signal induced by an S-wave source is absent, the electric IR is easier to be detected. Therefore an efficient method to detect different CO_2 saturations would be to measure the electric interfacial response using a S-wave source. The amplitude of the response would be up to 300 times higher than the amplitude of the signal induced by a water-saturated medium, depending on the model used for the CO_2-dependence of the electrokinetic, in the saturation range 5-15%, and 10 to 100 times higher in the 15-40% CO_2 saturation range.

7. Seismo-electromagnetic conversions induced in a CO_2 reservoir with a seal layer

Let us consider now a new model, shown in Figure 10, in which we intersperse a 10 m deep seal layer of very low permeability among a 100 m deep layer whose top boundary is the Air-Soil interface, and a semispace in which CO_2 saturation can be changed. Indeed clay layers can be present as thin intra-reservoir shales. They act as main barriers to the upward migration of CO_2 beneath which the the CO_2 accumulates at high saturations (Arts et al., 2004).

The three layers parameters are displayed in Table 3; we remark that the permeability of the seal layer is four orders of magnitude smaller than the one of the top layer and the semi-space. In order to better approximate a possible carbon dioxide deposition site, we strongly increase the NaCl concentration in the water saturating the semi-space, therefore enhancing its electrical conductivity, which yields a bulk conductivity of $\sigma = 0.12$ [S/m] at full water saturation. The semi-space is then the most electrically conductive, the seal layer has a smaller bulk conductivity including a surface conductivity, and the top layer has the lowest bulk conductivity. The zeta potential, which depends on the fluid conductivity is very small within the briny semi-space. It is about -3 mV

within the seal and -70 mV within the top layer. This configuration leads to an electrokinetic coupling in the seal layer about 16 times smaller than the value of the one corresponding to the top layer, and of about twice that of the semi-space. The electrokinetic coupling does not reflect here only the zeta potential (itself linked to the fluid conductivity), but also the permeability (see eq.3) which is very low in the half-space. Therefore the contrast in the electrokinetic coupling is higher between the semi-space and the seal layer than the one between the top layer and the seal layer.

According to the analysis performed in previous sections, an interface response is expected to arise at both seal interfaces, with potentially a larger signal between the semi-space and the seal layer because of a larger contrast in the electrokinetic couplings. However, the method is not expected to resolve them, because the two IR's are separated about 7 miliseconds (v_S=1700 m/s), the width of the central peak of the source being about 4.5 miliseconds. Recall, however, that we are not mainly interested in determining the width of the seal, but in what lies beneath it. Notice that previous numerical studies (Pride and Garambois, 2005) have shown that for thin enough layers, the Interface Response can attain very large values.

In Figure 11 we display a borehole gather for (a) the seismic waves, (b) the electric field and (c) the magnetic field, considering a 65% carbon dioxide saturation in the semispace. It can be seen in the leftmost picture that contrary to the seismic response of our first example, shown in Figure 2(a), the amplitude of the reflected seismic wave is much smaller than the incident wave, due to the similar mechanical properties of the seal layer and the semi-space, recall that they have just different permeabilities and different fluids saturating them. However, both electric interface response E_{IR} and magnetic interface response H_{IR} are clearly observable, raised simultaneously with the arrival of the incident seismic wave to the interface between the top and seal layers, at about 0.06 s. The electric IR can be detected within the whole depth range, whereas the magnetic IR can be detected only at depths below the seal layer. Also discernible is the coseismic magnetic field (see fig.11c), traveling within the incident, reflected and transmitted seismic shear waves.

With the goal of detecting possible changes in the CO_2 saturation within the semi-space, the magnetic and electric interfacial responses were calculated for CO_2 saturations of 5%, 25% and 65%. In Figure 12 we show time windows highlighting the difference between the magnetic field interface responses of two different CO_2 saturations; in (a) we take the difference between 65% and 5% saturations and in (b) we take the difference

between 65% and 25% saturations. The relative differences normalised by the value of the IR at 65% of CO_2 saturation (the maximum of the maxima of all traces is taken into account, as previousy explained) show a variation of 30% when saturation varies from 65% to 5%, and a variation of 22% when saturation varies from 65% to 25%. These results show us that even when the interface response of the bottom boundary of the seal is "entangled" with the one produced at its top boundary, the recorded magnetic IR in the well receivers -located below the lowest interface- are very sensitive to carbon dioxide saturation changes.

In Figure 13 we show the time windows highlighting the differences between the electric field interface responses of the same two different CO_2 saturations. The relative differences normalised by the value of the IR at 65% of CO_2 saturation show a variation of 62% when saturation varies from 65% to 5%, and a variation of 52% when saturation varies from 65% to 25%. Therefore the sensitivity of the electric IR to the CO_2 saturation variations is larger than the sensitivity of the magnetic IR.

The detection of the variation of CO_2 concentration could be therefore performed by measuring the electric and magnetic field in boreholes. The magnetic field measured below the interface could detect the magnetic IR induced by the contrast of the seal layer and the semi-space; the electric field could be measured below and above the interface. Moreover, as the coseismic part of the electric field is absent when using a S-wave source, the electric IR may be easier to be detected than the magnetic IR. However if the electric ambient noise is high, the electric IR may be still difficult to measure, even if a large variation is expected as a function of the CO_2 concentration. The measurement of the magnetic field below the interface may still help to detect the CO_2 saturation variations, because the magnetic IR is larger than the coseismic magnetic signal, and because of the sensitivity of the magnetic IR which is still noticeable although lower than the one of the electric IR.

8. Conclusions

-In this paper we numerically analyzed shear wave driven seismoelectromagnetic conversions in a surface-to-borehole layout, using a one dimensional finite elements code. Sensitivity analysis of the S-EM IR for porosity, permeability, zeta potential and viscosity were performed for a simple tabular medium, and normalized

responses were used in these analysis, in order to make them independent of the physical source used by the employed method.

-It was observed that -as expected- no contrast in the properties leads to the absence of interface response; and that the response increases when the contrast in porosity and zeta potential is increased, while for relatively large values of the viscosity the response is asymptotically constant.

-We studied also the behaviour of the electromagnetic responses for a model considering realistic partial CO_2 saturations. We used the extended Pride's formulation for the electrokinetic coupling for the case of partially saturated media recently presented in Warden et al. (2013) to take into account the presence of carbon dioxide in our model. Moreover, we studied the magnetic coseismic response and electric and magnetic interface responses using Perrier-Morat and Allègre formulas in the partial CO_2 saturation version of the electrokinetic coupling. We observed that the relative maximum in the interface response for both the electric and magnetic fields is different according to the different models of the CO_2-dependence for the electrokinetic coupling, and occurs at either around 10% or 70-90% of carbon dioxide saturation.

-These results are obtained assuming that the injection of supercritical CO_2 in water-saturated sandstone decreases the electrical conductivity, as shown by Borner et al. (2013) during short time experiments. However it has to be noted that the injection of supercritical CO_2 in brine solutions increases its electrical conductivity, because of the dissolution of CO_2 in water, with a larger effect on fresh water solution than on saline solutions (Borner et al., 2013). This effect was assumed not to take place in the short-time experiments. Therefore considering long-time period of CO_2 storage and dissolution process, further studies may consider different hypotheses on the effect of supercritical CO_2 on the electrical conductivity.

-When studying the magnetic and electric interface responses of a model for a sealed CO_2 reservoir with different saturations, we observed that they are sensitive to CO_2 saturation variations, even when they are superimposed with the interface response of the boundary between the overburden and the seal; the sensitivity of the electric IR is higher than the one of the magnetic IR. The electric IR variations are observable with recorders located in the reservoir above or below the seal layer, whereas the magnetic IR is only observed below the seal layer. Both magnetic and electric field measured in borehole could detect the variations of CO_2 saturation below the seal.

-Noting that up to now seismomagnetic signals were recorded in experiments performed in the laboratory by Bordes et al. (2008) or under special conditions (Gaffet et al., 2003), and further developments are needed to measure seismomagnetic signals in the field, we consider that an efficient method to detect a CO_2 saturation in the range 5-40% would be to measure the electric interfacial response using a S-wave source, expecting a signal 5 to 300 higher than the signal induced by a water-saturated medium.

-We expect the novel results presented in this work will be followed by other necessary developments, such as the analysis of the absolute amplitudes of the IR responses, to show if they are large enough to be detected. Moreover more realistic geological environments should be modeled, eventually leading to a new monitoring tool which complements the existing ones.

9. Acknowledgments

This work was partially supported by a CNRS (INSU) - CONICET international collaboration grant, and by Université de Strasbourg.

9. Bibliography

References

Aizawa, K., Uyeshima, M., Nogami, K., 2008. Zeta potential estimation of volcanic rocks on 11 island arc-type volcanoes in japan: implication for the generation of local self-potential anomalies. J. Geophys. Res. 113, B02201.

Allègre, V., Jouniaux, L., Lehmann, F., Sailhac, P., 2010. Streaming Potential dependence on water-content in fontainebleau sand. Geophys. J. Int. 182, 1248–1266.

Allègre, V., Lehmann, F., Ackerer, P., Jouniaux, L., Sailhac, P., 2012. Modelling the streaming potential dependence on water content during drainage: 1. A 1D modelling of SP using finite element method. Geophys. J. Int. 189, 285–295.

Arts, R., Eiken, O., Chadwick, A., Zweigel, P., van der Meer, L., Zinszner, B., july-august 2004. Monitoring of CO_2 injected at Sleipner using time lapse seismic data. Energy 19, 1383–1392.

Bale, R., Marchand, T., Wilkinson, K., Wikel, K., Kendall, R., 2013. The signature of shear-wave splitting: Theory and observations on heavy oil data. The Leading Edge 32 (1), 6434–6443.

Biot, M. A., March 1956a. Theory of propagation of elastic waves in a fluid-saturated porous solid: I. low frequency range. J. Acoust. Soc. Am. 28 (2), 168–178.

Biot, M. A., March 1956b. Theory of propagation of elastic waves in a fluid-saturated porous solid: Ii. high frequency range. J. Acoust. Soc. Am. 28 (2), 178–191.

Biot, M. A., January 1962. Mechanics of deformation and acoustic propagation in porous media. J. Appl. Phys. 34 (1), 36–40.

Block, G. I., Harris, J. G., 2006. Conductivity dependence of seismoelectric wave phenomena in fluid-saturated sediments. J. Geophys. Res. 111, B01304.

568 Bordes, C., Jouniaux, L., Garambois, S., Dietrich, M., Pozzi, J.-P., Gaffet, S., 2008. Evidence of the theoreti-
569 cally predicted seismo-magnetic conversion. Geophys. J. Int. 174, 489–504.

570 Borner, J., Herdegen, V., Repke, J., Spitzer, K., 2013. The impact of CO2 on the electrical properties of wa-
571 ter bearing porous media-laboratory experiments with respect to carbon capture and storage. Geophysical
572 Prospecting 61, 446–460.

573 Bourbié, T., Coussy, O., Zinszner, B., 1987. Acoustic of porous media. Institut Francais du pétrole publications
574 Ed. Technip.

575 Brie, A., Pampuri, F., Marsala, A., Meazza, O., 1995. Shear sonic interpretation in Gas Bearing sands. Society
576 of Petroleum Engineers.

577 Brovelli, A., Cassiani, G., Dalla, E., Bergamini, F., Pitea, D., Binley, A. M., 2005. Electrical properties of
578 partially saturated sandstones: Novel computational approach with hydrogeophysical applications. Water
579 resources research 41, 12pp.

580 Butler, K., Dupuis, J., Kepic, A., 2007. Signal to noise improvements in seismoelectrics data acquisition.
581 Ground and Borehole Geophysical Methods 111, 3753–3755.

582 Butler, K., Russell, R., Kepic, A., Maxwell, M., 1996. Measurements of the seismoelectric response from a
583 shallow boundary. Geophysics 61, 1769–1778.

584 Butler, K. E., Russell, R. D., 2003. Cancellation of multiple harmonic noise series in geophysical records.
585 Geophysics 68, 1083–1090.

586 Cairns, G., Jakubowics, H., Lonergan, L., Muggeridge, A., 2012. Using time-lapse seismic monitoring to
587 identify trapping mechanisms during CO_2 sequestration. International Journal of Greenhouse Gas Control
588 11, 316–325.

589 Carcione, J., Picotti, S., Gei, D., Michelini, R., 2012. Cross-hole electromagnetic and seismic modeling for CO_2
590 detection and monitoring in a saline aquifer. Journal of Petroleum Science and Engineering 100, 162–172.

591 Carcione, J., Picotti, S., Gei, D., Rossi, G., 2006. Physics and seismic modeling for monitoring CO_2 storage.
592 Pure and Applied Geophysics 163 (1), 175–207.

593 Chadwick, R., Noy, D., Arts, R., Eiken, O., 2009. Latest time-lapse seismic data from sleipner yield new
594 insights into co2 plume development. Energy Procedia 1 (1), 2103–2110.

595 Chadwick, R., Williams, G., Dellepine, N., Clochard, V., Labad, K., Sturton, S., Buddensiek, M., Dillen, M.,
596 Nikken, M., Lima, A. L., Arts, R., Neele, F., Rossi, G., 2010. Quantitative analysis of time-lapse seismic
597 monitoring data at the Sleipner CO_2 storage operation. The Leading Edge 29 (2), 170–177.

598 Chen, B., Mu, Y., sept 2005. Experimental studies of seismoelectric effects in fluid-saturated porous media. J.
599 Geophys. Eng. 2, 222–230.

600 Darwish, N., Hilal, N., 2010. A simple model for the prediction of CO_2 solubility in H_2-NaCl system at
601 geological sequestration conditions. Desalinization 260, 114–118.

602 Davis, T., Bibolova, A., O'Brien, S., Klepacki, D., Robinson, H., 2013. Prediction of residual oil saturation and
603 cap-rock integrity from time-lapse, multicomponent seismic data, Delhi Field, Louisiana. The Leading Edge
604 32 (1), 6434–6443.

605 Dupuis, J. C., Butler, K. E., Kepic, A. W., Nov-Dec 2007. Seismoelectric imaging of the vadose zone of a sand
606 aquifer. Geophysics 72, A81–A85.

607 Ellis, M., 2010. The potential of controlled source electromagnetic surveying in CO_2 storage monitoring. SEG
608 Expanded Abstracts 29, 843–847.

609 Fabriol, H., Bitri, A., Bourgeois, B., Delatre, M., Girard, J., Pajot, G., Rohmer, J., 2011. Geophysical methods
610 for CO_2 plume imaging: comparison of performances. Energy Procedia 4, 3604–3611.

611 Fischer, S., Liebscher, A., Lucia, M. D., Hecht, L., 2013. Reactivity of sandstone and siltstone samples from
612 the Ketzin pilot CO_2 storage site-Laboratory experiments and reactive geochemical modeling. Environmental
613 Earth Sciences 70, 3687–3708.

614 Gaffet, S., Guglielmi, Y., Virieux, J., Waysand, G., Chwala, A., Stolz, R., Emblanch, C., Auguste, M., Boyer,
615 D., Cavaillou, A., November 2003. Simultaneous seismic and magnetic measurements in the low-noise un-
616 derground laboratory (lsbb) of rustrel, france, during the 2001 january 26 indian earthquake. Geophys. J. Int.
617 155, 981–990.

618 Gao, Y., Hu, H., 2010. Seismoelectromagnetic waves radiated by a double couple source in a saturated porous
619 medium. Geophys. J. Int. 181, 873–896.

620 Garambois, S., Dietrich, M., 2001. Seismoelectric wave conversions in porous media: Field measurements and
621 transfer function analysis. Geophysics 66, 1417–1430.

622 Garambois, S., Dietrich, M., 2002. Full waveform numerical simulations of seismoelectromagnetic wave con-
623 versions in fluid-saturated stratified porous media. J. Geophys. Res. 107 (B7), ESE 5–1.

624 Girard, J., Coppo, N., Rohmer, J., Bourgeois, B., Naudet, V., Schmidt-Hattenberger, C., 2011. Time-lapse
625 csem monitoring of the ketzin (Germany) CO_2 injection using 2 x MAM configuration. Energia Procedia 4,
626 3322–3329.

627 Glover, P., Walker, E., Ruel, J., Tardif, E., 17p. 2012. Frequency-dependent streaming potential of porous
628 media-Part 2: Experimental mesurement of unconsolidated materials. Int. J. Geophysics 2012 (Hindawi
629 Publishing Corporation), Article ID 728495.

630 Gomez, J., Ravazzoli, C., 2011. AVA Seismic reflectivity analysis in carbon dioxide accumulations: sensitivity
631 to CO_2 phase and saturation. Journal of Applied Geophysics 72, 93–100.

632 Guan, W., Hu, H., 2008. Finite-difference modeling of the electroseismic logging in a fluid-saturated porous
633 formation. Journal of Computational Physics 227, 5633–5648.

634 Guan, W., Hu, H., Wang, Z., 2013. Permeability inversion from low-frequency seismoelectric logs in fluid-
635 saturated porous formations. Geophysical Prospecting 61, 120–133.

636 Guichet, X., Jouniaux, L., Catel, N., 2006. Modification of streaming potential by precipitation of calcite in a
637 sand-water system: laboratory measurements in the pH range from 4 to 12. Geophys. J. Int. 166, 445–460.

638 Guichet, X., Jouniaux, L., Pozzi, J.-P., 2003. Streaming potential of a sand column in partial saturation condi-
639 tions. J. Geophys. Res. 108 (B3), 2141.

640 Haartsen, M. W., Pride, S., 1997. Electroseismic waves from point sources in layered media. J. Geophys. Res.
641 102, 24,745–24,769.

642 Haines, S., 2004. Seismoelectric imaging of shallow targets. Ph.D. thesis, Stanford University.

643 Haines, S. H., Pride, S. R., 2006. Seismoelectric numerical modeling on a grid. Geophysics 71 (6), 57–65.

644 Haines, S. S., Pride, S. R., Klemperer, S. L., Biondi, B., March-April 2007. Seismoelectric imaging of shallow
645 targets. Geophysics 72, G9–G20.

646 Ishido, T., Mizutani, H., 1981. Experimental and theoretical basis of electrokinetic phenomena in rock water
647 systems and its applications to geophysics. J. Geophys. Res. 86, 1763–1775.

648 Ishido, T., Pritchett, J., Tosha, T., Nishi, Y., Nakanishi, S., 2013. Monitoring underground migration of se-
649 questered CO_2 using self-potential methods. Energy Procedia 37, 4077–4084.

650 Jackson, M. D., 2010. Multiphase electrokinetic coupling: Insights into the impact of fluid and charge distribu-
651 tion at the pore scale from a bundle of capillary tubes model. J. Geophys. Res. 115, B07206.

652 Johnson, D. L., Koplik, J., Dashen, R., 1987. Theory of dynamic permeability in fluid saturated porous media.
653 J. Fluid. Mech. 176, 379–402.

654 Jouniaux, L., Bordes, C., 2012. Frequency-Dependent Streaming Potentials: A Review. Int. J. Geophysics
655 vol.2012 (Hindawi Publishing Corporation), Article ID 648781, 11 p.

656 Jouniaux, L., Ishido, T., 16 p. 2012. Electrokinetics in Earth Sciences: a tutorial. Int. J. Geophysics vol.
657 2012 (Hindawi Publishing Corporation), Article ID 286107.

Jouniaux, L., Lallemant, S., Pozzi, J., 1994. Changes in the permeability, streaming potential and resistivity of a claystone from the Nankai prism under stress. Geophys. Res. Lett. 21, 149–152.

Jouniaux, L., Pozzi, J.-P., Berthier, J., Massé, P., 1999. Detection of fluid flow variations at the Nankai trough by electric and magnetic measurements in boreholes or at the seafloor. J. Geophys. Res. 104, 29293–29309.

Kazemeini, S., Juhlin, C., Fomel, S., 2010. Monitoring CO_2 response on surface seismic data; a rock physics and seismic modeling feasibility study at the CO_2 sequestration site, Ketzin, Germany. Journal of Applied Geophysics 71, 109–124.

Kiessling, D., Schmidt-Hattemberger, C., Schuett, H., Schilling, F., Krueger, K., Schoebel, B., Dankwardt, E., Kummerow, J., 2010. Geoelectrical methods for monitoring geological CO_2 storage: First results from cross-hole and surface-downhole measurements from the CO_2SINK test site at Ketzin (Germany). International Journal of Greenhouse Gas Control 4, 816–826.

Kim, J., Nam, M., Matsuoka, T., 2013. Estimation of CO_2 saturation during both CO_2 drainage and imbibition processes based on both seismic velocity and electrical resistivity measurements. Geophys. J. Int. electronical access July 9th.

Maineult, A., Jouniaux, L., Bernabé, Y., 2006. Influence of the mineralogical composition on the self-potential response to advection of kcl concentration fronts through sand. Geophys. Res. Lett. (33), L24311.

Martens, S., Kempka, T., Liebscher, A., Lüth, S., Möller, F., Myrttinen, A., Norden, B., Schmidt-Hattenberger, C., Zimmer, M., Kühn, M., 2012. Europe's longest-operating on-shore CO_2 storage site at Ketzin,Germany: a progress report after three years of injection. Environ Earth Sci 67, 323–334.

Martens, S., Liebscher, A., Möller, F., Henninges, J., Kempka, T., Lüth, S., Norden, B., Prevedel, B., Szizybalski, A., Zimmer, M., Kühn, M., the Ketzin Group, 2013. CO_2 storage at the Ketzin pilot site, Germany: Fourth year of injection, monitoring, modeling and verification. Energy Procedia 37, 6434–6443.

Mikhailov, O. V., Queen, J., Toksöz, M. N., 2000. Using borehole electroseismic measurements to detect and characterize fractured (permeable) zones. Geophysics 65, 1098–1112.

682 Moore, J., Glaser, S., Morrison, H., 2004. The streaming potential of liquid carbon dioxide in berea sandstone.
683 Geophys. Res. Lett. 31, L17610.

684 Perrier, F., Morat, P., 2000. Characterization of electrical daily variations induced by capillary flow in the
685 non-saturated zone. Pure Appl. Geophys. 157, 785–810.

686 Pozzi, J.-P., Jouniaux, L., 1994. Electrical effects of fluid circulation in sediments and seismic prediction. C.R.
687 Acad. Sci. Paris, serie II 318 (1), 73–77.

688 Pride, S., 1994. Governing equations for the coupled electromagnetics and acoustics of porous media. Phys.
689 Rev. B: Condens. Matter 50, 15678–15695.

690 Pride, S., Garambois, S., 2005. Electroseismic wave theory of frenkel and more recent developments. Journal
691 of Engineering Mechanics, 898–907.

692 Pride, S., Haartsen, M. W., 1996. Electroseismic wave properties. J. Acoust. Soc. Am. 100, 1301–1315.

693 Pride, S., Morgan, F. D., 1991. Electrokinetic dissipation induced by seismic waves. Geophysics 56 (7), 914–
694 925.

695 Pride, S. R., 2005. Relationships between Seismic and Hydrological Properties. Vol. 50. Springer Netherlands.
696 URL http://www.springerlink.com/content/h1167431tnm23135/abstract/

697 Reppert, P. M., Morgan, F. D., Lesmes, D. P., Jouniaux, L., 2001. Frequency-dependent streaming potentials. J.
698 Colloid Interface Sci. (234), 194–203.

699 Revil, A., Linde, N., Cerepi, A., Jougnot, D., Matthäi, S., Finsterle, S., 2007. Electrokinetic coupling in unsat-
700 urated porous media. J. Colloid Interface Sci. 313, 315–327.

701 Ringrose, P., Atbi, M., Mason, D., Espinassous, M., Myhrer, O., Iding, M., Mathieson, A., Wright, I., 2009.
702 Plume development around well KB-502 at the In Salah co_2 storage site. First Break 27, 85–89.

703 Santos, J., Ravazzoli, C., Gauzellino, P., Carcione, J., Cavallini, F., 2004. Simulation of waves in poro-
704 viscoelastic rocks saturated by immiscible fluids. Numerical evidence of a second slow wave. Journal of
705 Computational Acoustics 12, 1–21.

706 Schakel, M., Smeulders, D., Slob, E., Heller, H., 2011. Seismoelectric interface response: Experimental results
707 and forward model. Geophysics 76, N29–N36.

708 Schakel, M., Smeulders, D., Slob, E., Heller, H., 2012. Seismoelectric fluid/porous-medium interface response
709 model and measurements. Transport in Porous media 93, 271–282.

710 Schoemaker, F., Smeulders, D., Slob, E., 2007. Simultaneous determination of dynamic permeability and
711 streaming potential. SEG expanded abstracts 26, 1555–1559.

712 Strahser, M., Jouniaux, L., Sailhac, P., Matthey, P.-D., Zillmer, M., 2011. Dependence of seismoelectric ampli-
713 tudes on water-content. Geophys. J. Int. 187, 1378–1392.

714 Teja, A. S., Rice, P., 1981. Generalized corresponding states method for the viscosities of liquid mixtures. Ind.
715 Eng. Chem. Fund. 20 (1), 77–81.

716 Thibeau, S., Mucha, V., 2011. Have we overestimated saline aquifer CO_2 storage capacities? Oil Gas Sci.
717 Technol. Rev. IFP Energies nouvelles 66 (1), 81 – 92.

718 Thompson, A. H., Gist, G. A., 1993. Geophysical applications of electrokinetic conversion. The Leading Edge
719 12, 1169–1173.

720 Vinogradov, J., Jaafar, M., Jackson, M. D., 2010. Measurement of streaming potential coupling coefficient in
721 sandstones saturated with natural and artificial brines at high salinity. J. Geophys. Res. 115, B12204.

722 Vinogradov, J., Jackson, M., 2011. Multiphase streaming potential in sandstones saturated with gas/brine and
723 oil/brine during drainage and imbibition. Geophys. Res. Lett. 38, L01301.

724 Wang, Z., Small, M., Karamalidis, A., 2013. Multimodel predictive system for carbon dioxide solubility in
725 saline formation waters. Environmental Science and Technology 47, 1407–1415.

726 Warden, S., Garambois, S., Jouniaux, L., Brito, D., Sailhac, P., Bordes, C., 2013. Seismoelectric wave propa-
727 gation numerical modeling in partially saturated materials. Geophys. J. Int. 194, 1498–1513.

728 Warden, S., Garambois, S., Sailhac, P., Jouniaux, L., Bano, M., 2012. Curvelet-based seismoelectric data
729 processing. Geophys. J. Int. 190, 1533–1550.

730 Wiese, B., Böhner, J., Enachescu, C., Würdemann, H., Zimmermann, G., 2010. Hydraulic characterisation
731 of the stuttgart formation at the pilot test site for CO_2 storage, Ketzin, Germany. International Journal of
732 Greenhouse Gas Control 4, 960–971.

733 Wiese, B., Zimmer, M., Nowak, M., Pellizzari, L., Pilz, P., 2013. Well-based hydraulic and geochemical
734 monitoring of the above zone of the CO_2 reservoir at Ketzin, Germany. Environmental Earth Sciences 70,
735 3709?3726.

736 Zhang, F., Juhlin, C., Cosma, C., Tryggvason, A., 2012. Cross-well seismic waveform tomography for moni-
737 toring CO_2 injection: a case study from the ketzin site, Germany. Geophys. J. Int. 189, 629–646.

738 Zhu, Z., Haartsen, M. W., Toksöz, M. N., 1999. Experimental studies of electrokinetic conversions in fluid-
739 saturated borehole models. Geophysics 64, 1349–1356.

740 Zyserman, F., Gauzellino, P., Santos, J., 2010. Finite element modeling of SHTE and PSVTM electroseismics.
741 J. Applied Geophysics 72, 79–91.

742 Zyserman, F., Gauzellino, P., Santos, J., 2012. Numerical evidence of gas hydrate detection by means of elec-
743 troseismics. J. Applied Geophysics 86, 98–108.

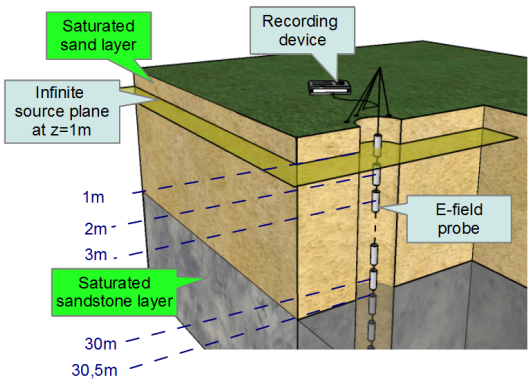

Figure 1: *Tabular model and seismoelectric vertical profiling layout. The subsurface consists of a fully saturated 30.5 m thick sandstone layer on top of a saturated sand half-space. The source is oriented along y, 51 dipole receivers -set 1 m apart- are deployed inside a vertical uncased borehole.*

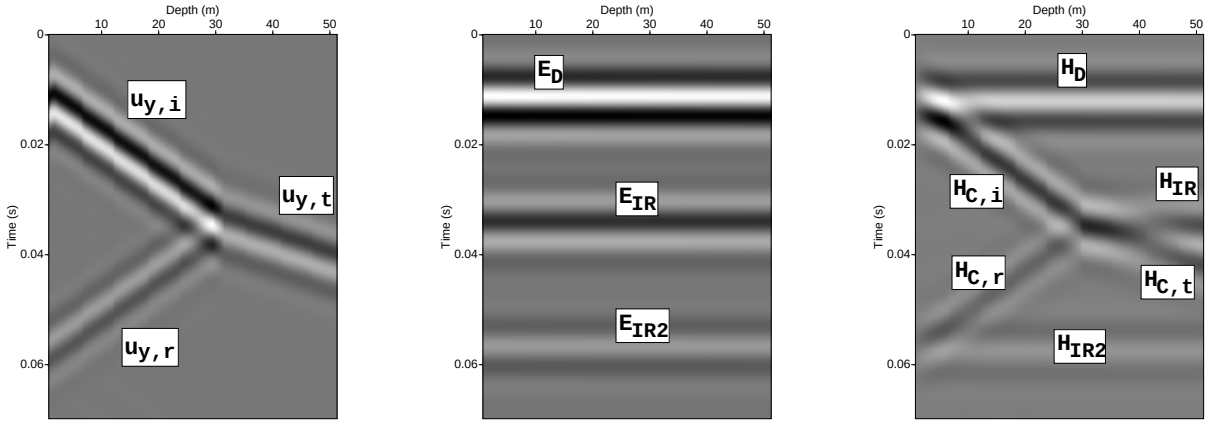

(a) (b) (c)

Figure 2: *Results obtained with the FE-algorithm using an infinite source along y, as described in Section 4.1. (a) Horizontal solid displacement $u_{y,j}$, j = i,r,t, i: incident, r: reflected, t: transmitted, (b) Horizontal electric field E_y, subscript D stands for direct, i.e. the field originated as a convertion at the source; subscript IR is associated to the interface response generated at 30.5 m depth, and the signal with subscript IR2 is assumed to be an interface response generated at the surface when $u_{y,r}$ reaches it at about 0.057 s, (c) horizontal magnetic Field H_x; the subscript D stands for direct, C for coseismic (i: incident, r: reflected and t: transmitted), subscript IR is associated to the magnetic interface response generated at 30.5 m depth, IR2 is the interface response generated at the surface, when $u_{y,r}$ reaches it.*

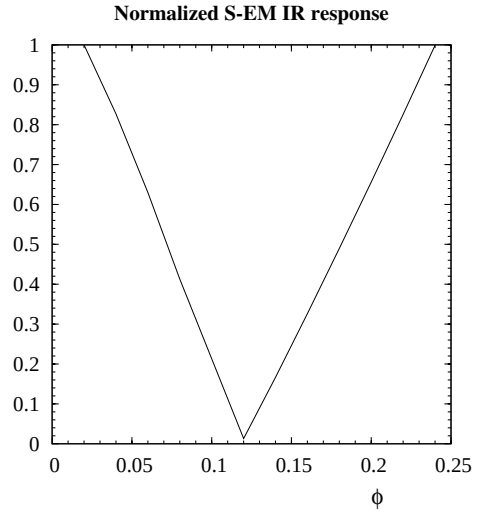

Figure 3: *Maximum S-EM IR amplitude versus porosity in the half-space of model described in Section 5.1.*

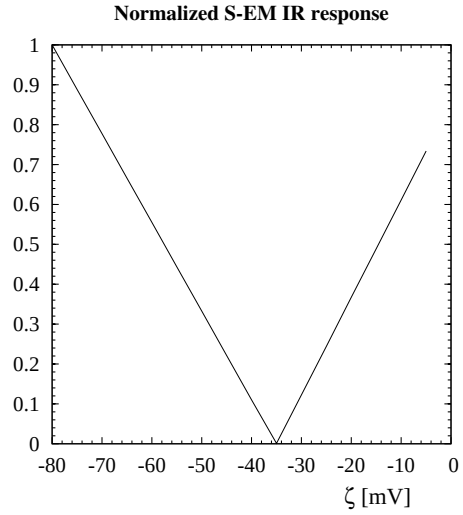

Figure 4: *Maximum S-EM IR amplitude versus ζ potential in the half-space of model described in Section 5.2.*

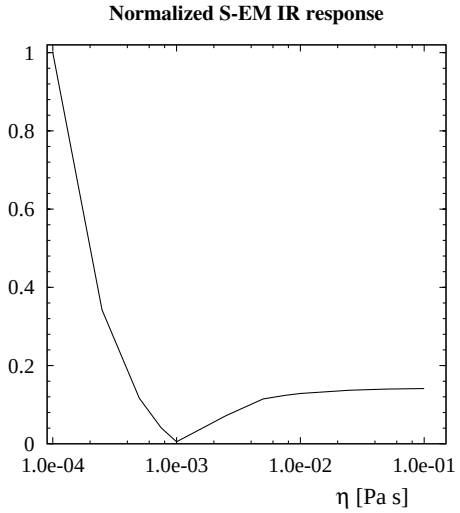

Figure 5: *Maximum S-EM IR amplitude versus viscosity η in the half-space of model described in Section 5.3.*

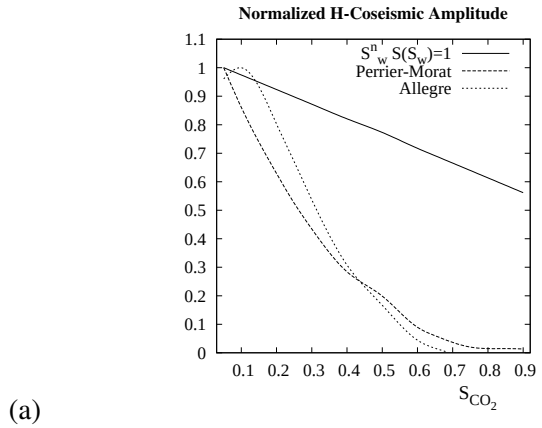

(a)

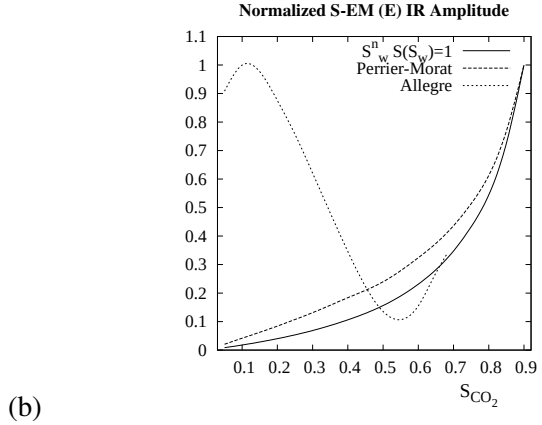

(b)

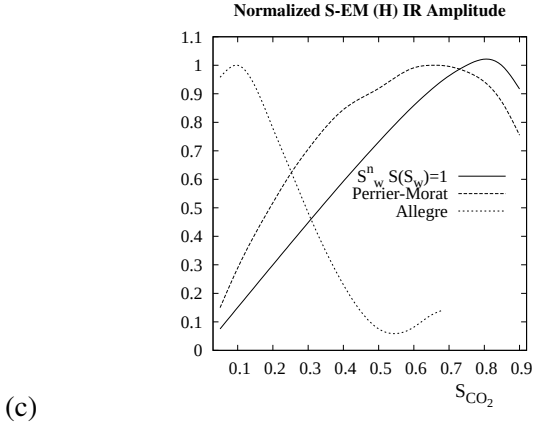

(c)

Figure 6: *CO_2 saturation dependence of the (a) Coseismic Magnetic Response, (b) S-EM Interface Response for the electric field and (c) S-EM Interface Response for the magnetic field for the different electrokinetic coupling models assumed in this work.*

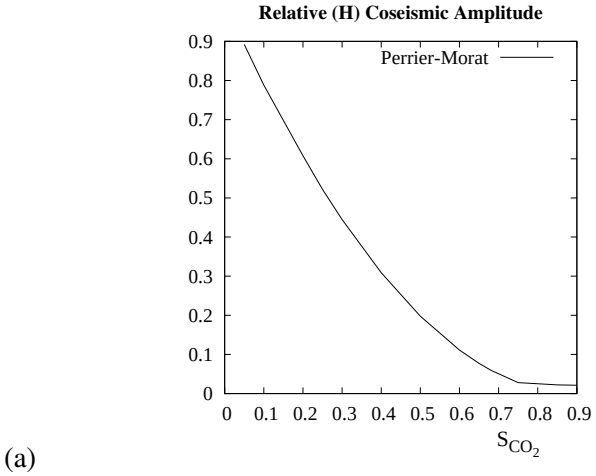

(a)

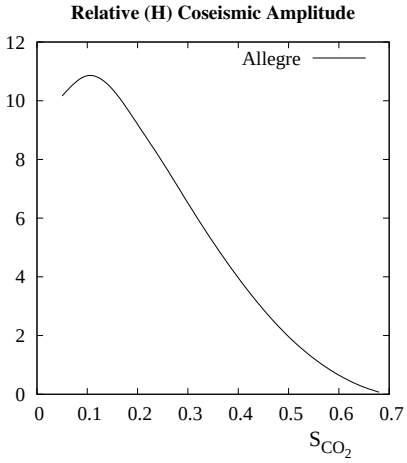

(b)

Figure 7: *Relative amplitude of the coseismic magnetic field for (a) Perrier-Morat model and (b) Allègre model; both cases are compared to the amplitude of the H-coseismic response when using the electrokinetic coupling* L_0 *assuming* $S_w^n S(w) = 1$ *in Eq.13.*

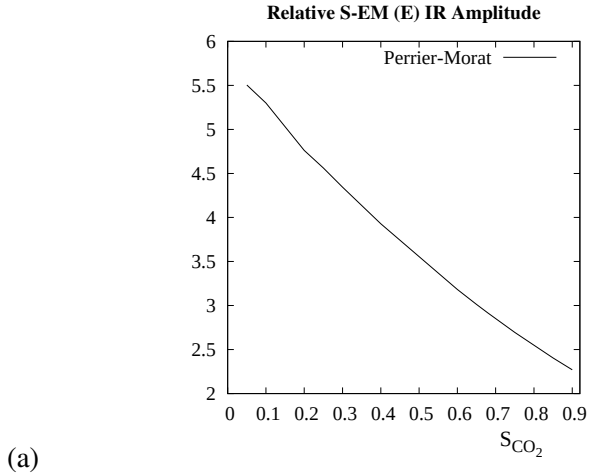

(a)

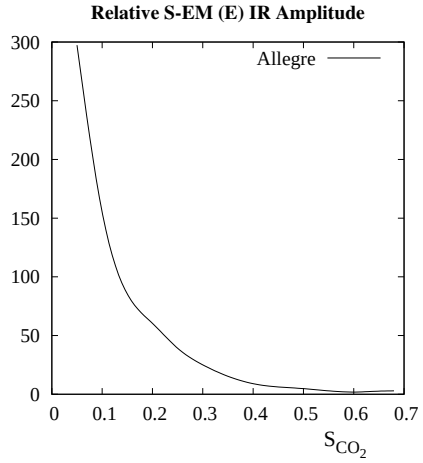

(b)

Figure 8: *Relative amplitude of the Interface Response electric field for (a) Perrier-Morat model and (b) Allègre model; both cases are compared to the amplitude of the S-EM (E) response when using the electrokinetic coupling* L_0 *assuming* $S_w^n S(w) = 1$ *in Eq.13.*

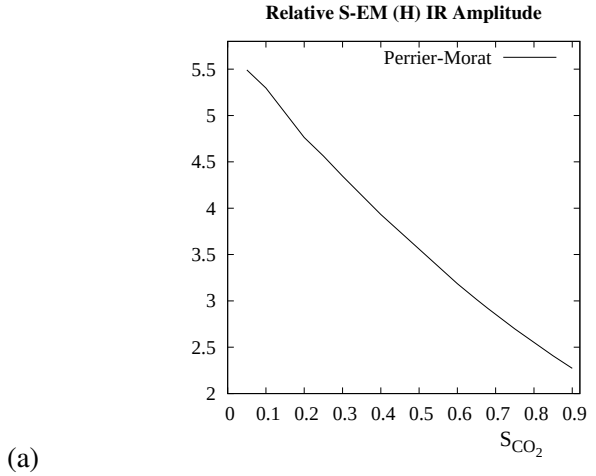

(a)

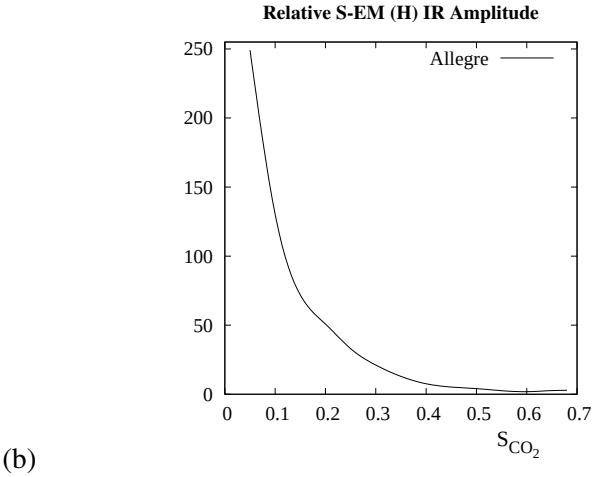

(b)

Figure 9: *Relative amplitude of the Interface Response magnetic field for (a) Perrier-Morat model and (b) Allègre model; both cases are compared to the amplitude of the S-EM (H) response when using the electrokinetic coupling L_0 assuming $S_w^n S(w) = 1$ in Eq.13.*

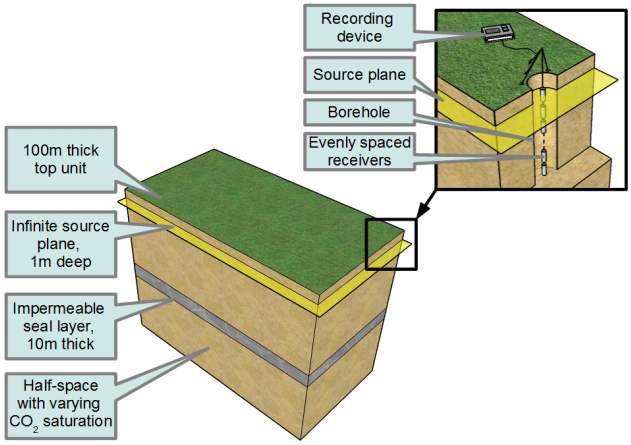

Figure 10: *Model with a seal layer.*

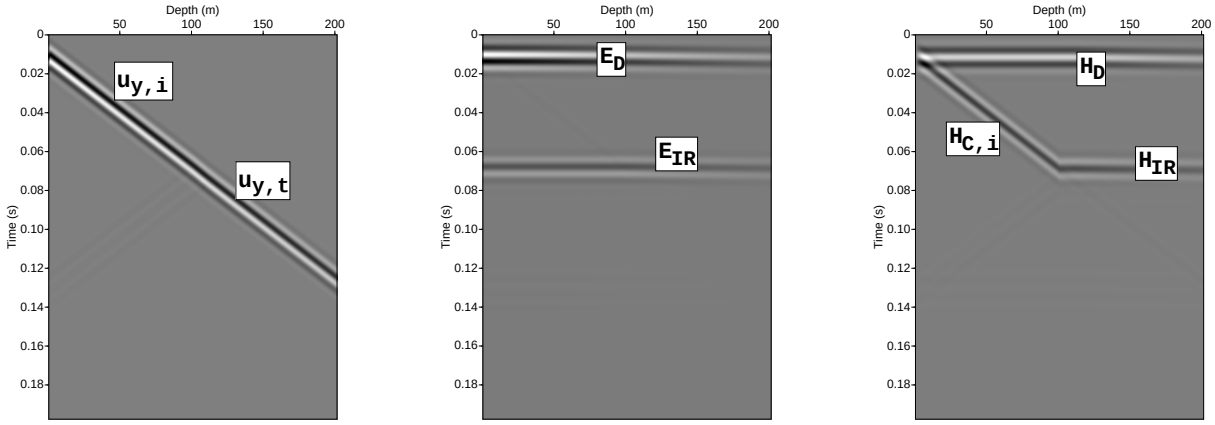

(a) (b) (c)

Figure 11: *Results for the model of CO_2 reservoir with a seal layer. CO_2 saturation is 65% within the semi-space (below depth 100m). Horizontal displacement u_y (a), horizontal electric field E_y (b) and horizontal magnetic Field H_x (c) obtained with the FE-algorithm using an infinite source along y, as described in Section 4.1.*

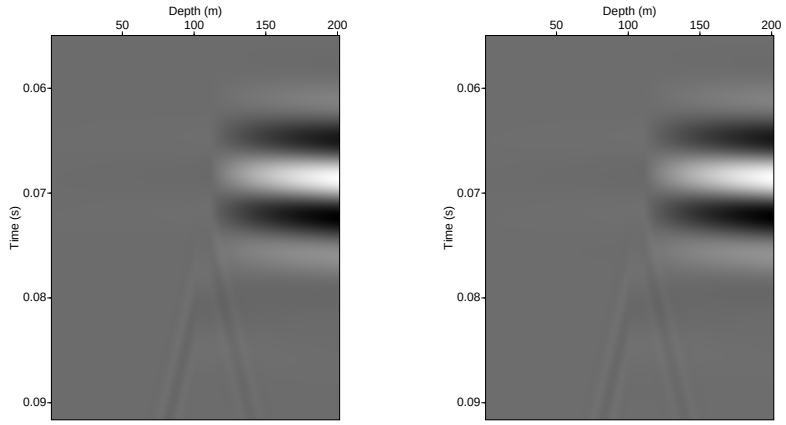

(a) (b)

Figure 12: *From the magnetic field well gather, -Figure 11(c)- we select a time window, displaying the difference of the magnetic field IR response between two different CO_2 saturations, namely 5% and 65% (a); while in (b) the same result as in (a) is displayed, but the difference is taken considering CO_2 saturations of 25% and 65%.*

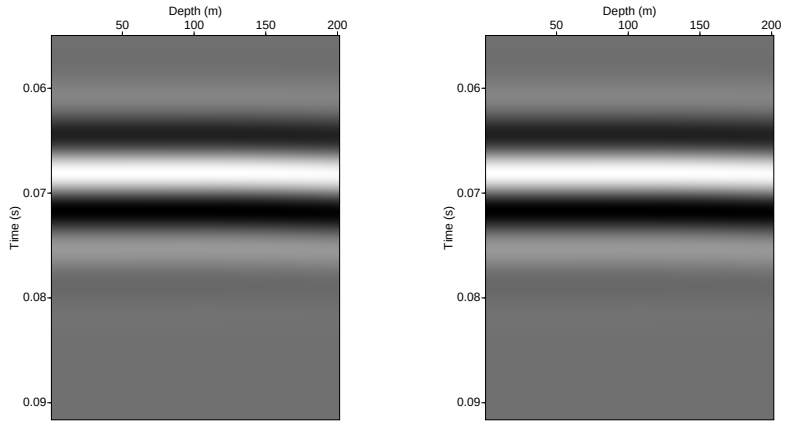

(a) (b)

Figure 13: *From the electric field well gather, -Figure 11(b)- we select a time window, displaying the difference of the electric field IR response between two different CO_2 saturations, namely 5% and 65% (a); while in (b) the same result as in (a) is displayed, but the difference is taken considering CO_2 saturations of 25% and 65%.*

	Sand	**Sandstone I**	**Sandstone II**
ϕ (%)	35	20	12
m	2.05	1.70	1.7
k_0 (m^2)	10^{-11}	10^{-13}	4.32×10^{-13}
k_s (Pa)	36×10^9	36×10^9	36×10^9
k_f (Pa)	2.27×10^9	2.27×10^9	2.27×10^9
k_{fr} (Pa)	2.92×10^9	14.40×10^9	18.45×10^9
G_{fr} (Pa)	2.49×10^9	14.08×10^9	20.38×10^9
v_S (m/s)	1104	2485	2909
v_P (m/s)	2344	4017	4529
v_{EM} (m/s)	8.69×10^5	1.03×10^6	3.1×10^6
η_w (Pa.s)	1×10^{-3}	1×10^{-3}	1×10^{-3}
η_g (Pa.s)	1.8×10^{-5}	1.8×10^{-5}	1.8×10^{-5}
ρ_s (Kg/m^3)	2.6×10^3	2.6×10^3	2.6×10^3
ρ_w (Kg/m^3)	1×10^3	1×10^3	1×10^3
ρ_g (Kg/m^3)	1	1	1
C_0 (mol/L)	1×10^{-3}	1×10^{-3}	1×10^{-3}
σ (S/m)	1.59×10^{-3}	1.14×10^{-3}	1.2×10^{-4}
ζ (V)	-0.07	-0.07	-0.07
κ_w	80	80	80
κ_s	4	4	4
κ_g	1	1	1
T (K)	298	298	298

Table 1: *First two columns correspond to properties of the model described in Section 4.1, whilst the third one to the model used in Section 5. Seismic and electromagnetic velocities are calculated at the source peak frequency of 120 Hz.*

ϕ (%)	2	4	6	8	10	12
k_0 (m^2)	0	1.09×10^{-15}	2.79×10^{-14}	1.28×10^{-13}	2.50×10^{-13}	4.32×10^{-13}
ϕ (%)	14	16	18	20	22	24
k_0 (m^2)	6.86×10^{-13}	1.02×10^{-12}	1.46×10^{-12}	2.00×10^{-12}	2.66×10^{-12}	3.46×10^{-12}

Table 2: *Permeability values associated with porosity values ranging from 2 to 24 % computed using the empirical laws of Bourbié et al. (1987).*

	Top layer	**Seal**	**Semispace**
ϕ (%)	20	20	20
m	1.7	1.7	1.7
k_0 (m^2)	0.5×10^{-13}	0.4×10^{-17}	0.5×10^{-13}
k_s (Pa)	36×10^9	36×10^9	36×10^9
k_{fr} (Pa)	5.40×10^9	5.40×10^9	5.40×10^9
G_{fr} (Pa)	5.80×10^9	5.80×10^9	5.80×10^9
ρ_s (Kg/m^3)	2.6×10^3	2.6×10^3	2.6×10^3
κ_s	4	4	4
k_w (Pa)	2.27×10^9	2.27×10^9	2.27×10^9
η_w (Pa.s)	1×10^{-3}	1×10^{-3}	1×10^{-3}
ρ_w (Kg/m^3)	1×10^3	1×10^3	1×10^3
κ_w	80	80	80
C_0 (mol/L)	1×10^{-3}	4×10^{-2}	0.4
k_{CO_2} (Pa)	—	—	25×10^6
η_{CO_2} (Pa.s)	—	—	1.5×10^{-5}
ρ_{CO_2} (Kg/m^3)	—	—	505
κ_{CO_2}	—	—	1
σ (S/m)	3.41×10^{-4}	1.55×10^{-3}	* 0.12
ζ (V)	-0.07	-0.027	-0.0023
T (K)	298	298	298

Table 3: *Properties of the model analysed in Section 7, the * value for the electrical conductivity for the semispace corresponds to the water saturated case; the value for an effective fluid mixture with S_{CO_2}=65% is equal to* 1.59×10^{-2}

Appendix A. One dimensional SHTE equations

Consider Pride's equations in the equivalent form given in Zyserman et al. (2012)

$$(\sigma + i\epsilon\omega)E - \nabla \times H + L(\omega)\eta_f k^{-1}(\omega)\left[i\omega u^f - L(\omega)E\right] = -J_e^{ext}, \tag{A.1}$$

$$\nabla \times E + i\omega\mu H = -J_m^{ext}, \tag{A.2}$$

$$-\omega^2\rho_b u^s - \omega^2\rho_f u^f - \nabla\cdot\tau(u) = F^{(s)}, \tag{A.3}$$

$$-\omega^2\rho_f u^s + \eta_f k^{-1}(\omega)\left[i\omega u^f - L(\omega)E\right] + \nabla p_f = F^{(f)}, \tag{A.4}$$

$$\tau_{lm}(u) = 2G_{fr}\,\varepsilon_{lm}(u^s) + \delta_{lm}\left(\lambda_c\,\nabla\cdot u^s + \alpha K_{av}\,\nabla\cdot u^f\right), \tag{A.5}$$

$$p_f(u) = -\alpha K_{av}\,\nabla\cdot u^s - K_{av}\nabla\cdot u^f. \tag{A.6}$$

Here τ and ε are the stress and strain tensors, $\rho_b = \phi\rho_f + (1-\phi\rho_s)$ the bulk density, K_{av} is the fluid-storage coefficient and αK_{av} is the Biot coupling coefficient, with $\alpha = 1 - K_{fr}/K_s$. In the seismic frequency regime, for most fluid saturated rocks, displacement currents can be safely neglected against conduction currents in the factor multiplying the electric field E in the first term of Eq.(A.1). Besides, as it has been demonstrated (Haines and Pride, 2006), if $\eta L^2(\omega)/(\sigma k(\omega)) \ll 1$, the electroosmotic feedback can be neglected in Biot's equations, and the latter decouples from Maxwell's equations. As we are dealing with just seismic shear sources, we set the electromagnetic sources, and the seismic source acting upon the fluid to zero, J_m^{ext}=J_e^{ext}=$F^{(f)}$=0. Moreover, as $F^{(s)}$ is considered to be a shearing force parallel to the y axis acting on a horizontal infinite plane upon a horizontally layered Earth, only solid displacements $u^s = u_y^s(z,\omega)$ and fluid displacements $u^f = u_y^f(z,\omega)$ are possible. Therefore, we have $E = E_y(z,\omega)$ and $H = H_x(z,\omega)$. Under these considerations, Eq.(A.1)-Eq.(A.6) can be rewritten as

$$\sigma E - \partial_z H = i\omega\eta_f k^{-1}(\omega)L(\omega)u^f, \tag{A.7}$$

$$\partial_z E + i\omega\mu H = 0 \tag{A.8}$$

$$-\omega^2\rho_b u^s - \omega^2\rho_f u^f - \partial_z\left(G_{fr}u^s\right) = F^s, \tag{A.9}$$

$$-\omega^2\rho_f u^s + i\omega\eta_f k^{-1}(\omega)\,u^f = 0, \tag{A.10}$$

where we used ∂_z to denote the derivative with respect to z. Notice that in, although we have not considered it, in the seismic frequency range it is usual to take the low frequency limit for the electrokinetic coupling coefficient and the dynamic permeability; in this case we would have $i\omega(\eta_f/k_0)L_0u^f$ as the r.h.s. of Eq. (A.7) and $i\omega\eta_f\, k^{-1}(\omega) \approx (-\omega^2 g_0 + i\omega\eta/k_0)$ in Eq. (A.10); in this last expression g_0 is the mass coupling coefficient. Finally, following Santos et al. (2004), we express $F^{(s)}$ as

$$F^{(s)}(z,\omega) = F(\omega)\partial_z\delta(z - z_f). \tag{A.11}$$

Here $F(\omega)$ is the Fourier transform of the source time signature, and the Dirac's delta derivative must be understood in the distributional sense; by z_f we denote the depth at which the source is located. The set of equations (A.7)-(A.10) must be completed with appropriate boundary conditions. For Maxwell's equations we use absorbing boundary conditions (ABC's) at the top and bottom boundaries, for Biot's equations we use the free boundary condition for the air-soil interface and again ABC's at the bottom boundary; see Zyserman et al. (2010, 2012) and references therein for details. In the present case they read, for Maxwell's equations and Biot's equations respectively:

$$(1-i)\sqrt{\frac{\sigma}{2\omega\mu}}E - \nu H = 0, \tag{A.12}$$

where ν takes the value -1 at the top boundary and the value 1 at the bottom one,

$$\partial_z u^s = 0 \qquad \text{Top boundary}, \tag{A.13}$$

$$-G_{fr}\partial_z u^s = i\omega(\rho_b - \rho_f^2/g(\omega))\sqrt{\frac{G_{fr}}{\rho_b - \rho_f^2/g(\omega)}}, \qquad \text{Bottom boundary}, \tag{A.14}$$

where $g(\omega) = (1/\omega)\mathrm{Im}(\eta/k(\omega))$. As already stated, the system of equations (A.7)-(A.14) is solved by means of a finite elements procedure.